

Supporting Information for

Angstrom-Size Defect Creation and Ionic Transport through Pores in Single-Layer MoS₂

*Jothi Priyanka Thiruraman^{1,2‡}, Kazunori Fujisawa^{3‡}, Gopinath Danda^{1,2}, Paul Masih Das¹,
Tianyi Zhang⁵, Adam Bolotsky³, Néstor Perea-López³, Adrien Nicolai⁶, Patrick Senet⁶, Mauricio
Terrones^{3,4,5}, Marija Drndić^{1*}*

¹Department of Physics and Astronomy and ² Department of Electrical and Systems Engineering, University of Pennsylvania, Philadelphia, Pennsylvania 19104, United States

³Department of Physics, Center for 2-Dimensional and Layered Materials, ⁴Department of Chemistry, and ⁵Department of Materials Science and Engineering, The Pennsylvania State University, University Park, Pennsylvania 16802, United States

⁶Laboratoire Interdisciplinaire Carnot de Bourgogne UMR 6303 CNRS-Université de Bourgogne Franche Comté, 9 Avenue Alain Savary, BP 47870, F-21078 Dijon Cedex, FRANCE.

‡ These authors contributed equally to this work

*E-mail, drndic@physics.upenn.edu.

Table of Contents

1. Fabrication of MoS₂ Devices
2. Transfer of Single-Layer MoS₂ onto Carbon Grids
3. Control of Defects by Varying the Ga⁺ Ion Dose
4. Raman/Photoluminescence Spectroscopy of Irradiated Membranes
5. AC-STEM Observation and Counting of Defects from AC-STEM Images
6. Simulation of HAADF Images of Defects
7. Statistical Analysis of the Sub-nm size pores using AC-STEM Images
8. Ionic Current Measurements
9. Calculation of Effective Diameters of Non-Circular Pores
10. Non-Equilibrium Molecular Dynamics (NEMD)

1. Fabrication of MoS₂ Devices

A 50-nm thick suspended window of silicon nitride of dimensions 50 $\mu\text{m} \times 50 \mu\text{m}$ was fabricated on a 5 $\mu\text{m}/525 \mu\text{m}$ SiO₂/Si wafer using optical lithography and KOH and HF wet etching techniques^{1,2}. A 200-nm-diameter hole was drilled in the center of the window using a 30 kV, 10 pA Ga⁺ FIB source and a single-layer MoS₂ flake was transferred onto it using a custom-built manipulator (**Figure S2**) to form a suspended MoS₂ membrane.

2. Transfer of Single-Layer MoS₂ onto Carbon Grids:

To transfer single-layer MoS₂ onto gold Quantifoil TEM grid (from SPI), a layer of poly methyl methacrylate (PMMA) (495K, A4) was first spin-coated onto as-grown MoS₂ flakes. After PMMA cured, it was immersed in 2M NaOH etchant solution to lift off the PMMA-coated MoS₂ flakes. Subsequently, the detached film was rinsed in deionized water and fished onto the grid. Finally, PMMA layer was cleaned in acetone and IPA, leaving the transferred single-layer MoS₂ on the grid.

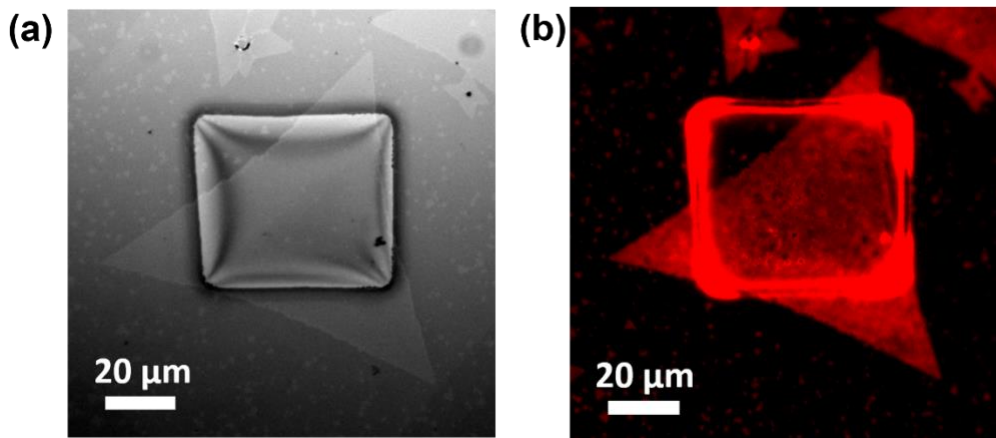


Figure S1. (a) Optical and (b) fluorescence (673 nm-centered bandpass filtered) microscopic image of transferred single-layer MoS₂ flake onto SiN_x window with FIB hole at the center.

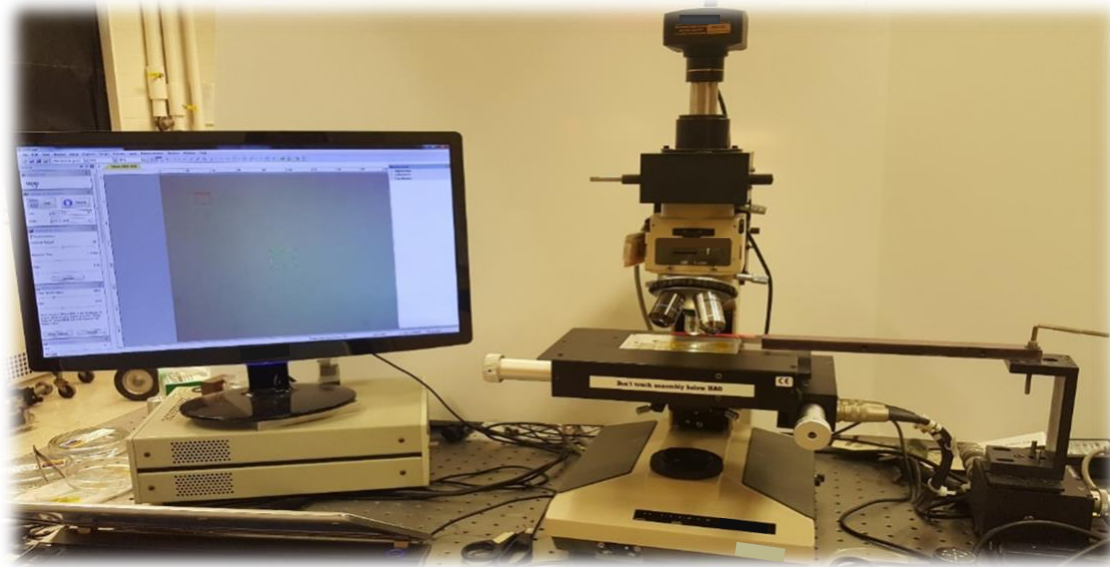


Figure S2. The setup of the deterministic transfer stage for micro-positioning MoS₂ flakes onto SiN_x windows. A micromanipulator consisting of a piezoelectric stage (NanoMax-TS flexure stage, Thorlabs) and a custom-built cantilever was applied to align the MoS₂ sample with SiN_x. An optical microscope (Olympus BH2 Microscope) was used to monitor the deterministic transfer process.

3. Control of Defects by varying Ga⁺ Ion Dose

Suspended MoS₂ flakes were irradiated with Ga⁺ ions using the ion gun of a FEI Helios dual beam instrument. To perform the Ga⁺ ion irradiation, we set the acceleration voltage at 30 kV and the current intensity at 230 pA. The beam incidence was normal to the surface and followed a raster path over a rectangular area, 410 μm long and 274 μm wide. The beam impinges the sample in imaging mode, in this condition the beam dwelled 50 ns in each step; the spacing between steps was approximately 260 nm. Finally, the different doses on the single-layer MoS₂ were achieved by manually varying the irradiation time.

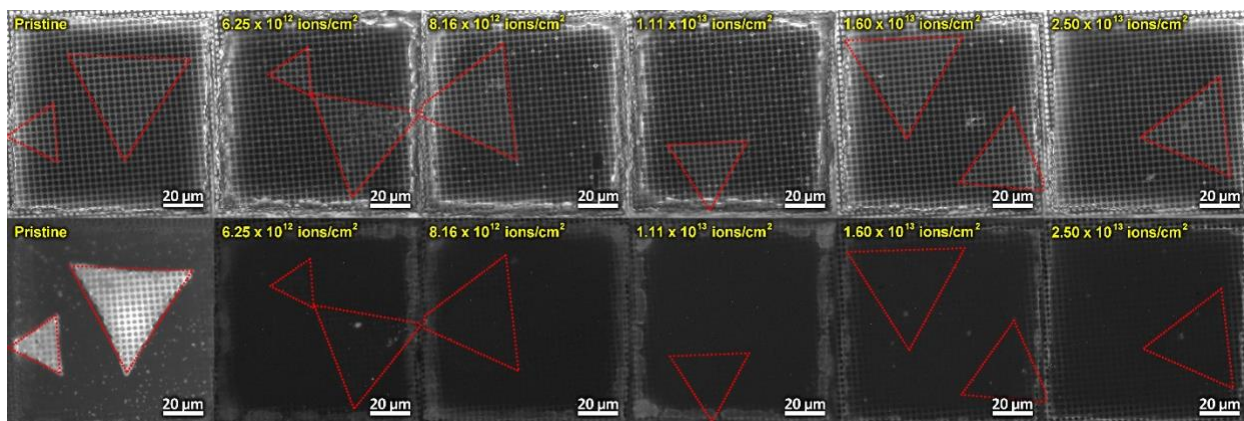


Figure S3. Optical images (top) and fluorescence images (bottom, 673 nm-centered bandpass filtered) of the pristine and the Ga^+ ion irradiated single-layer MoS_2 on Quantifoil TEM grid.

4. Raman/Photoluminescence Spectroscopy of Irradiated Membranes

All Raman spectra and photoluminescence spectra were collected from suspended MoS_2 flakes over Quantifoil TEM grid. To avoid both heating effect and laser induced damage to the suspended MoS_2 , 10-50 μW of laser power under $\times 100$ (N.A. 0.95) objective lens was used. The Raman and Photoluminescence spectra were acquired using the ‘inVia Raman Microscope’ (Renishaw) equipped with a 488 nm laser.

5. AC-STEM Observation and Counting Defects from AC-STEM Images

Aberration corrected scanning transmission electron microscopy (AC-STEM) study was carried out by FEI Titan³ G2 S/TEM operated at 80 kV to investigate the atomic structure of MoS_2 triangles. A high-angle annular dark field (HAADF) detector was used for Z contrast imaging. In order to reduce noise and increase visibility of atoms, Gaussian Blur filter with 0.03 nm of blurring width was applied by ImageJ program. Prior to vacancy-defect counting from STEM-HAADF images, further noise reduction was applied using the “Remove Outliers” process. At this point STEM-HAADF signal from sulfur atoms were spread. Cleaned STEM-HAADF images were then

subjected to the “Local Threshold” process with the Sauvola method to obtain binary STEM-HAADF images which consist of black-colored defect regions and white-colored MoS₂ regions. Statistical analysis of the defect area and the number of defects were carried out using these binary STEM-HAADF images.

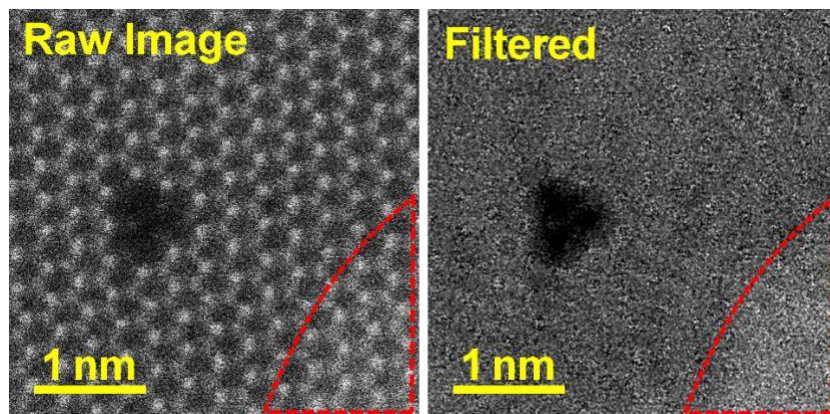


Figure S4. Raw STEM image of a V_{3Mo+5S} type vacancy-defect in MoS₂ lattice (left). The periodic feature of MoS₂ lattice was removed by applying several circular band pass filters to FFT (right). The highlighted area by red-line corresponds to the carbon deposited area.

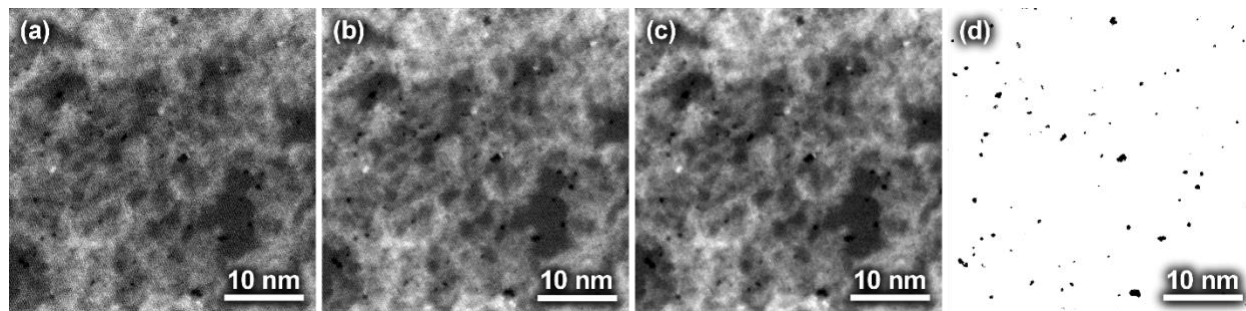


Figure S5. Step-by-step images of the binary creation process from the raw STEM images. The ImageJ software was used for all processing. A raw STEM image ((a), 38.4 nm × 38.4 nm, 2048 pixel × 2048 pixel) is processed using the *Gaussian Blur* filter (filtering radius: 0.03 nm) to reduce noise (b). Further, noise reduction is applied by using the *Remove Outliers* process (10 pixel of radius and threshold 50 was used) (c). After this step, the ADF signal from Mo and S are dispersed, then the crystal and defect parts are separated. Finally, to efficiently ignore the carbon contamination layer present on the surface of MoS₂, *Local Threshold* process (*Sauvola* method, radius: 40 pixel, *k*-value: 0.20, *r*-value: 200) is applied, and then the binary image is obtained (d).

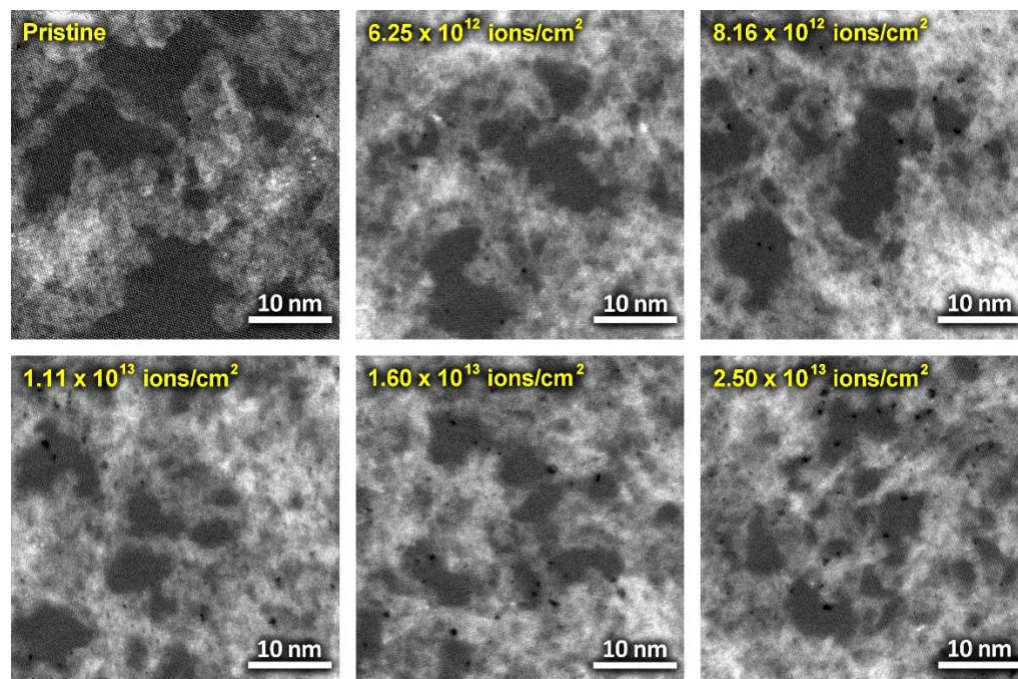


Figure S6. Low magnification STEM-HAADF image of the pristine and Ga⁺ ion irradiated MoS₂.

6. Simulation of HAADF Images of Defects

The STEM-ADF image simulation was conducted by the QSTEM package³. Simulation parameters such as acceleration voltage, spherical aberration (C_3 and C_5), convergence angle and inner and outer angles for HAADF detector were set according to experimental conditions. All other aberrations except spherical aberration and defocus were kept as 0.

7. Statistical Analysis of the Sub-nm size pores using AC-STEM Images

In order to investigate the effect of the Ga⁺ ion dose on nanopore area and density, statistical analysis was applied to AC-STEM images. Binary images were first prepared from AC-STEM images by post-image processing (see Figure S5). Nanopore density (Figure S7(a)), average area

(Figure S7(b)) and total pore area percentage (Figure S7(c)) increase linearly with irradiation dose. By extrapolating the linear regression (Figure S7(c)), an *atom sputtering rate* was calculated as 1.07 atom/ion. The area of the pore slightly increases when the Ga⁺ ion dose is increased, but since the pore area is limited by the atomic configuration, a Gaussian distribution is not expected. By comparing the average and the median of the nanopore area (Figure S7(b)), only the average increased when the Ga⁺ ion dose increased to 2.50×10^{13} ions/cm², indicating that some pores expanded or merged laterally. Therefore, the nanopore diameter distribution was obtained (Figure S7(d)). Instead of the average nanopore area, S (nm²), the effective nanopore diameter, D (nm), was calculated from the area using $S = \pi(D/2)^2$. The pore diameter distribution showed that diameters of most defective samples were several angstroms in size.

Further, to understand the distribution of nanopore diameters, the same nanopore counting procedure was applied to simulated STEM-HAADF images. The simulated STEM-HAADF images (Figure S7(e)) were acquired using parameters from the actual imaging conditions. The effect of six different nanopore structures—three types of single-Mo-based nanopores (V_{1Mo} (0.38 nm), V_{1Mo+3S} (0.56 nm), V_{1Mo+6S} (0.56 nm)) and three types of double-Mo-based nanopores (V_{2Mo+2S} (0.54 nm), V_{2Mo+6S} (0.68 nm), $V_{2Mo+10S}$ (0.70 nm))—were considered, and the diameter for each nanopore was obtained using the simulated STEM-HAADF images. These were also plotted in the nanopore diameter distribution (see bars in Figure S7(d), the color of the bar corresponds to the nanopore structure in inset of Figure S7(d)). Since the nanopore counting procedure was carried out at low magnification (Figure S6), the effect of mono-sulfur vacancies exhibiting low STEM-HAADF intensities at the edges of nanopores, was mostly ignored. This leads to the conclusion that the diameter of V_{1Mo+3S} is almost the same as the diameter of V_{1Mo+6S} . When we compare experimental diameter distributions with simulated diameters for V_{1Mo}

nanopores, a large number of nanopores exhibit diameters smaller than the V_{1Mo} pores. In order to understand this difference, we counted the number of missing Mo atoms from high magnification STEM-HAADF images (Figure S8).

For the lowest irradiation dose (6.25×10^{12} ions/cm²), 80% of the defects consist of single-Mo-based nanopore, indicating that the overall nanopore diameter distribution shifted to smaller diameters, possibly due to broadening of atoms by higher order aberrations in the STEM-HAADF image. Assuming that a random number of surrounding sulfur atoms are sputtered along with a molybdenum atom by Ga⁺ ion irradiation, and that the sputtering probability for sulfur atoms is low, V_{1Mo} and V_{2Mo+2S} can be a major contribution to the nanopore distribution.

For 6.25×10^{12} ion/cm² irradiations, the main peak in the pore diameter distribution is close to the V_{1Mo} , whereas the density of nanopores with diameter corresponding to 0.54 nm (diameter for simulated V_{2Mo+2S}), is low. As the Ga⁺ ion dose increased, the nanopore density centered at nanopore diameters of 0.54 nm increased, indicating that the density of double-Mo-based pores increased. Moreover, when the Ga⁺ ion dose reached 2.50×10^{13} ion/cm², densities of pores with size > 0.8 nm in diameter increased.

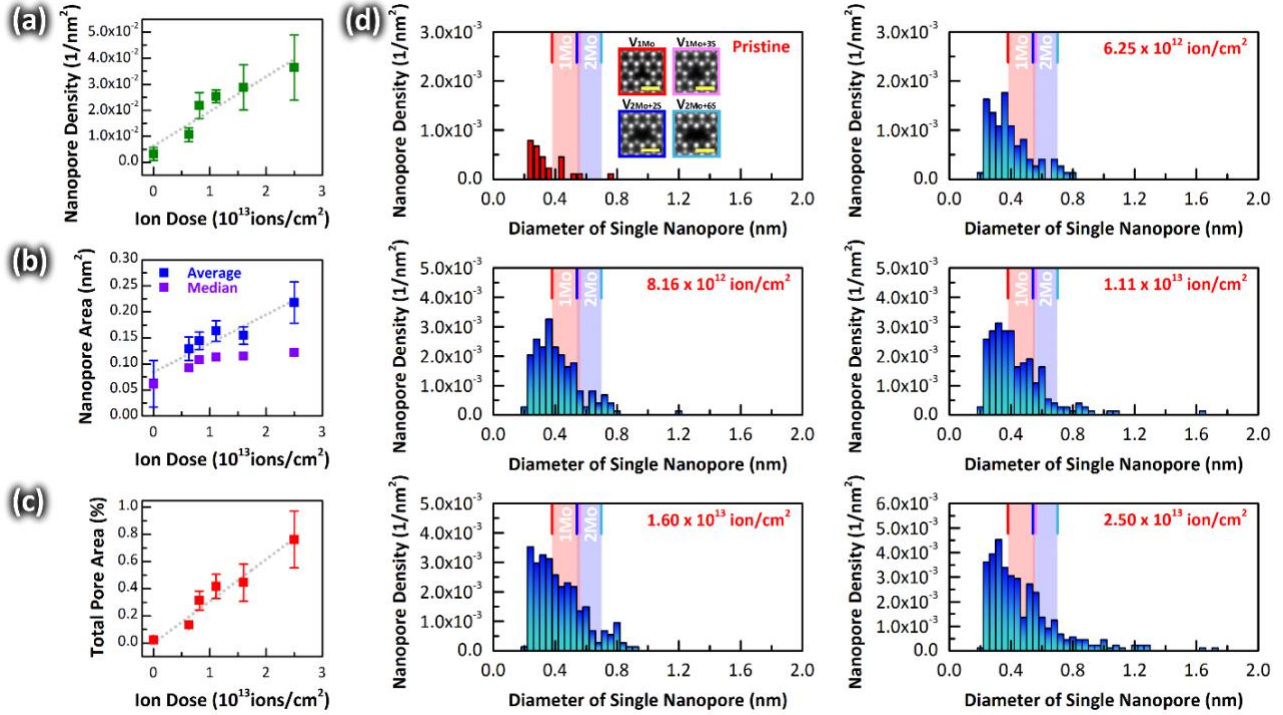


Figure S7. Statistical analysis of sub-nm diameter pores identified by AC-STEM observation. (a) pore density, (b) pore area and (c) total pore area percentage were calculated from binary images created from AC-STEM image. (d) Distribution of the pore diameters for defects produced by Ga^+ ion irradiation, for different Ga^+ ion doses. The red (blue)-colored box corresponds to diameter ranges for $V_{1\text{Mo}+y\text{S}}$ ($V_{2\text{Mo}+y\text{S}}$) pores which is calculated from simulated STEM-HAADF images by a commercial software, QSTEM (inset, scale bar is 500 pm).

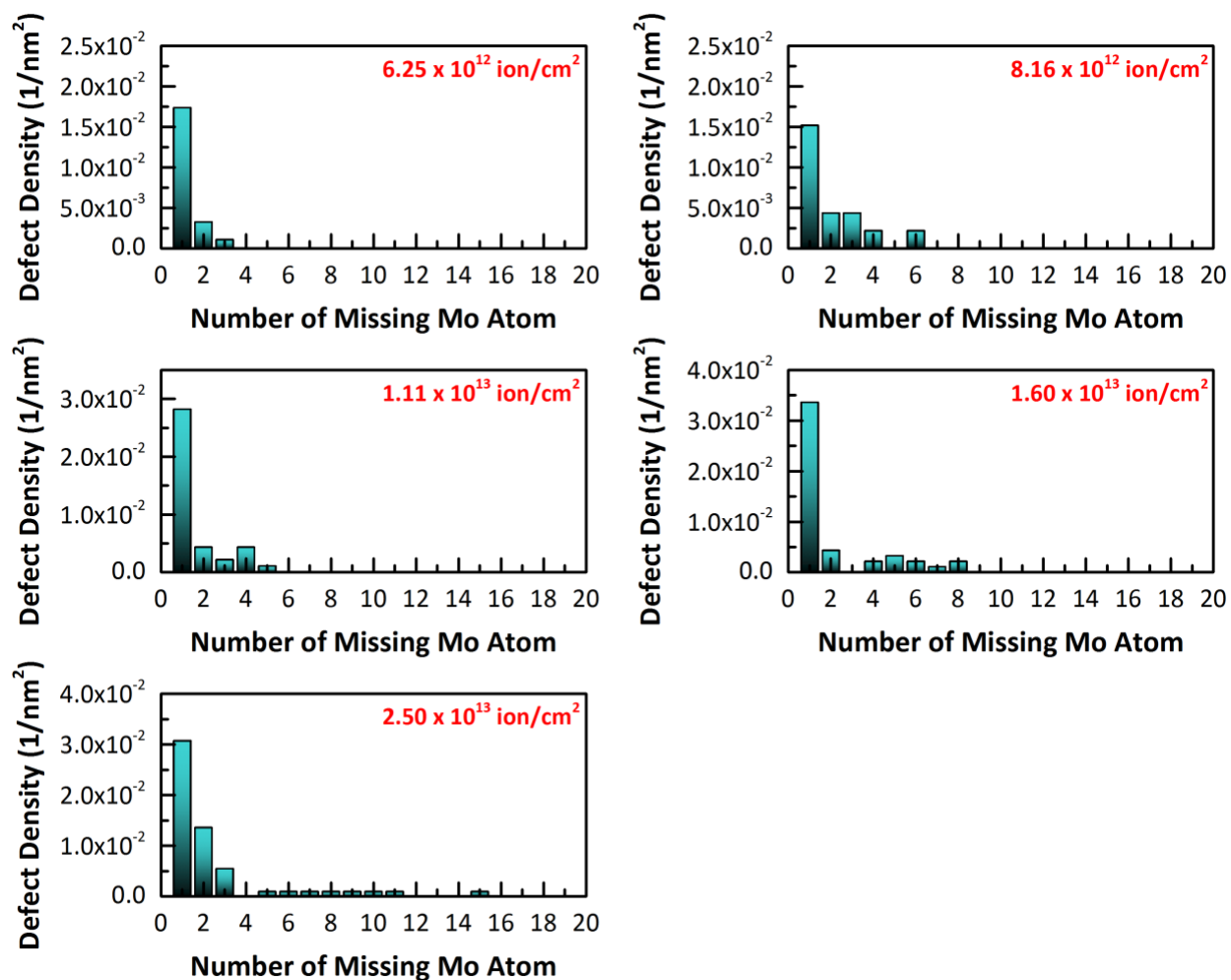


Figure S8. Statistical analysis of missing Mo atom using high magnification the STEM-HAADF images.

8. Ionic Current Measurements

EPC-10 HEKA amplifier with Ag/AgCl electrodes was used to perform ionic measurements on our devices. 1 M KCl (with 10 mM EDTA and 1 mM Tris; measured solution conductivity = 11.18 S/m, pH 8.7) solution was prepared using DI water, and the conductivity and pH were measured with Accumet XL-20 pH conductivity meter. Ionic measurements were conducted on pristine samples (non-irradiated, MoS₂ suspended samples) and irradiated samples. Prior to ionic

measurements, the device was annealed at 300° C in an Ar-H₂ environment for 90 minutes. This was a crucial step as it was found to prevent delamination of the flakes when the device interacts in a liquid environment. The device was then immersed in a 50% water-ethanol solution for at least 30 minutes to help in wetting and formation of ionic channels through the defects^{1,2}. 1 M KCl solution was then introduced on both sides of the device and a voltage bias (V_B) was applied while simultaneously measuring the ionic current (I_B). To ensure no damage to our devices during ionic experiments, V_B was kept between ± 0.5 V for most of our devices.

9. Calculation of Effective Diameters of Non-Circular Pores

In order to define an effective diameter, we measured the total sub-nm diameter pore area using a threshold function from a commercial, ImageJ software, and then calculated the diameter that corresponds to a circle with an equivalent area. For TEM images (MoS₂ pore 1 and pore 2), the scale bar used was derived from the averaged distances between two adjacent Molybdenum atoms (0.32 nm) in the vicinity of the pore.

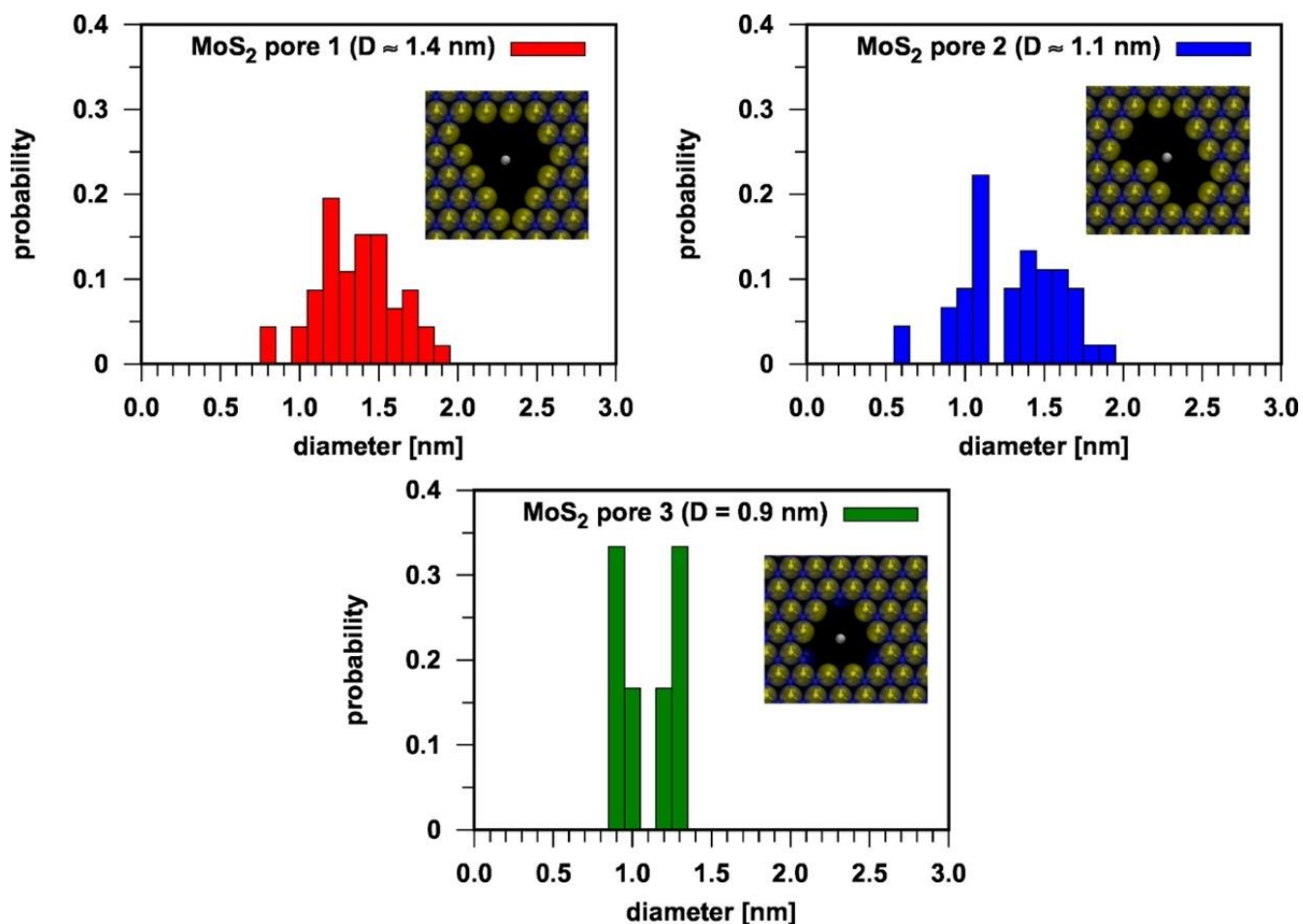


Figure S9. Distributions of diameters computed from MoS₂ pores atomic structures. The center of mass of the pore is shown using a grey sphere in the structure images in inset.

10. Non-Equilibrium Molecular Dynamics (NEMD)

Simulations were performed using the LAMMPS software package.⁴ The simulation box of dimension 7.5 x 7.5 x 15 nm³ is comprised of a MoS₂ nanoporous membrane plus a 1M KCl ionic solution. A Stillinger-Weber potential is used to characterize Mo-S bonded interactions⁵ and non-bonded interactions between MoS₂, water and ions were described using a Lennard-Jones (LJ) plus Coulomb potential. The water model used in the present work is the TIP3P model.⁶ LJ parameters for K⁺ and Cl⁻ ions were taken from references,⁷ where specific parameters were developed for the

water model employed. LJ parameters and bulk partial charge for Mo and S atoms were taken from references respectively,^{8,9} as already used in other works.¹⁰ Before running NEMD, an equilibrium of the system in the NPT ensemble ($T = 300\text{K}$ and $P = 1\text{ bar}$) without any electric field was performed during 100 ps to relax the system at the target temperature and pressure. Relaxation was followed by MD runs of 10 ns carried out in the NVT ensemble using the velocity-Verlet algorithm¹¹ with a time step of 1 fs. A Nosé-Hoover thermostat^{12,13} was used to maintain the temperature at 300 K with a time constant of 0.1 ps. Particle-particle particle-mesh method¹⁴ was used to describe long-range electrostatic interactions. A cutoff of 1.0 nm was applied to LJ and Coulomb potential for non-bonded interactions. A SHAKE algorithm¹⁵ was used to constrain the bond lengths and angle of TIP3P water molecules. Finally, Non-Equilibrium MD simulations (NEMD) using periodic boundary conditions were carried out by applying an external uniform electric field, directed normal to the nanoporous membrane (z-direction), acting on all charged particles throughout the simulated system. This gives rise to a force $q_i \cdot E$ that is applied to all the atoms in the simulation box, *i.e.*, Mo, S, O_w, H_w, K⁺ and Cl⁻. The resulting applied voltage is $V = -EL_z$, where L_z is the length of the simulation box in the z-direction, with $V = 0.15, 0.3, 0.45$ and 0.6 V . The ionic current and conductance calculations were performed using the same method as described in previous work.¹⁶

REFERENCES

- (1) Danda, G.; Masih Das, P.; Chou, Y.-C.; Mlack, J. T.; Parkin, W. M.; Naylor, C. H.; Fujisawa, K.; Zhang, T.; Fulton, L. B.; Terrones, M.; Johnson, A. T. C.; Drndić, M. *ACS Nano* **2017**, *11*(2), 1937-1945.
- (2) Liu, K.; Feng, J.; Kis, A.; Radenovic, A. *ACS Nano* **2014**, *8* (3), 2504–2511.
- (3) Koch, C. Determination of Core Structure Periodicity and Point Defect. *PhD. Thesis*, Arizona State University, May **2002**.
- (4) Plimpton, S. *J. Comput. Phys.* **1995**, *117* (1), 1–19.
- (5) Jiang, J.-W. *Nanotechnology* **2015**, *26* (31), 315706.
- (6) Jorgensen, W. L.; Chandrasekhar, J.; Madura, J. D.; Impey, R. W.; Klein, M. L. *J. Chem. Phys.* **1983**, *79* (2), 926–935.
- (7) Suk Joung, I.; Cheatham, J. *Phys. Chem. B*, 2008, *112* (30), 9020–9041
- (8) Liang, T.; Phillpot, S. R.; Sinnott, S. B. *Phys. Rev. B - Condens. Matter Mater. Phys.* **2009**, *79* (24), 1–14.
- (9) Varshney, V.; Patnaik, S. S.; Muratore, C.; Roy, A. K.; Voevodin, A. A.; Farmer, B. L. *Comput. Mater. Sci.* **2010**, *48* (1), 101–108.
- (10) Heiranian, M.; Farimani, A. B.; Aluru, N. R. *Nat. Commun.* **2015**, *6*, 8616.
- (11) Swope, W. C.; Andersen, H. C.; Berens, P. H.; Wilson, K. R. *J. Chem. Phys.* **1982**, *76* (1), 637–649.
- (12) Nosé, S. *J. Chem. Phys.* **1984**, *81* (1), 511–519.
- (13) Hoover, W. G. *Phys. Rev. A* **1985**, *31* (3), 1695–1697.
- (14) Hockney, R.W.; Eastwood, J.W *Computer Simulation using Particles*; Adam- hilger: New York, **1989**
- (15) Ryckaert, J. P.; Ciccotti, G.; Berendsen, H. J. C. *J. Comput. Phys.* **1977**, *23* (3), 327–341.
- (16) Perez, B.; Senet, P.; Meunier, V.; Nicolai, A. *WSEAS Trans. Circuits Syst.* **2017**, *16*, 35–44.